Depth selective magnetic phase coexistence in FeRh thin films

APL Materials

Depth selective magnetic phase coexistence in FeRh thin films

Cite as: APL Mater. **8**, 121103 (2020); https://doi.org/10.1063/5.0032130
Submitted: 06 October 2020 . Accepted: 16 November 2020 . Published Online: 15 December 2020

W. Griggs, B. Eggert, M. O. Liedke, M. Butterling, A. Wagner, U. Kentsch, E. Hirschmann, M. Grimes, A. J. Caruana, C. Kinane, H. Wende, R. Bali, and T. Thomson

Depth selective magnetic phase coexistence in FeRh thin films

Cite as: APL Mater. 8, 121103 (2020); doi: 10.1063/5.0032130
Submitted: 6 October 2020 • Accepted: 16 November 2020 •
Published Online: 15 December 2020

W. Griggs,[1,a] B. Eggert,[2] M. O. Liedke,[3] M. Butterling,[3] A. Wagner,[3] U. Kentsch,[4] E. Hirschmann,[3] M. Grimes,[1,b] A. J. Caruana,[5] C. Kinane,[5] H. Wende,[2] R. Bali,[4] and T. Thomson[1]

AFFILIATIONS

[1]NEST Research Group, Department of Computer Science, The University of Manchester, Oxford Road, Manchester M13 9PL, United Kingdom
[2]Faculty of Physics and Center for Nanointegration Duisburg-Essen (CENIDE), University of Duisburg-Essen, Lotharstr. 1, 47057 Duisburg, Germany
[3]Institute of Radiation Physics, Helmholtz-Zentrum Dresden-Rossendorf, Bautzner Landstr. 400, 01328 Dresden, Germany
[4]Institute of Ion Beam Physics and Materials Research, Helmholtz-Zentrum Dresden-Rossendorf, Bautzner Landstr. 400, 01328 Dresden, Germany
[5]ISIS, Science and Technology Facilities Council, Rutherford Appleton Laboratory, Harwell Science and Innovation Campus, Didcot, Oxon OX11 0QX, United Kingdom

[a]**Author to whom correspondence should be addressed:** william.griggs@manchester.ac.uk
[b]**Current address:** Laboratory for Mesoscopic Systems, Department of Materials, ETH Zurich, 8093 Zurich, Switzerland and Laboratory for Multiscale Materials Experiments, Paul Scherrer Institute, 5232 Villigen PSI, Switzerland.

ABSTRACT

We demonstrate the manipulation of magnetic phases in FeRh thin films through atomic displacements and the distribution of structural defects. Atomic scale disorder can be controlled via irradiation with light noble gas ions, producing depth-varying nanoscale phase configurations of distinct antiferromagnetic, ferromagnetic, and paramagnetic regions. Here, we perform a spatial characterization of the magnetic phases and the local magnetic environment around the Fe atoms, as well as the variation of the open-volumes around atomic sites. Thus, a direct correspondence between the existence of the three magnetic phases and lattice defects is revealed. By careful selection of the irradiating fluence, we show that it is possible to produce simple and thermally stable magnetic configurations, such as uniform magnetization or a bilayer phase structure. Furthermore, the thin film surface and interfaces are observed as the nucleation sites for the transitions between the phases. These results demonstrate a sensitive nanoscale manipulation of magnetic properties, shedding light on magnetic ordering in alloy lattices and broadening the scope for applications.

INTRODUCTION

The ability to selectively modulate intrinsic magnetic properties at the nanoscale is critical for the development of spintronic and data storage devices with improved efficiency. For these applications, equiatomic FeRh with a B2 structure emerges as a natural candidate material, owing to its first-order metamagnetic phase transition (MPT) from antiferromagnetic (AF) to ferromagnetic (FM) ordering at temperatures modestly above ambient.[1] The onset temperature and interval of the MPT can be manipulated by varying the stoichiometry,[2] magnetic field,[3–6] impurity species and concentration,[7–10] epitaxial[11–13] or induced[14–21] strains, or local disorder.[22,23] This large range of tunability options opens the door toward functional devices where the coupling between phases can be engineered to provide switching with enhanced stability,[24,25] single-electrode magnetic tunnel junctions,[26] or ultrafast dynamics via spin pumping.[27] However, for these applications to be realized, it is critical that the relative distribution of AF, FM, and paramagnetic (PM)

regions can be manipulated with both the lateral and vertical resolution, either by careful optimization of the growth process or by using post-fabrication processing methods.

The modification of lattice ordering at atomic scale, such as through site-swapping,[28] sub-unit cell atomic displacements,[29] or vacancies,[30] has been used as an effective technique to change the magnetic characteristics of various thin film systems, where usually the objective is to convert a FM region to a nonmagnetic state such as for patterned recording media.[31–36] Local manipulation of the magnetic behavior of B2-ordered lattices such as B2 $Fe_{60}Al_{40}$ and B2 $Fe_{50}Rh_{50}$ can be achieved by the application of focused ion-irradiation, focused laser-pulsing, or nanoindentation. Each approach has its specific advantages, for instance, laser processing can provide all-laser reversible magnetization switching[22] or the precision placement of magnetic domain pinning centers using nanoindentation.[23] Here, we investigate the depth variation of the magnetization realized by broad-beam irradiation of B2 FeRh. The resulting depth variation of M_s can help to relate the magnetic properties to the nature and concentration of defects, which is valuable information for designing embedded nanomagnets using focused ion-beams.[37]

It has been shown in various research studies that in addition to the thermally driven MPT in FeRh, there is a disorder-induced MPT from AF to FM ordering. Moreover, with further lattice disordering, an additional phase transition to PM behavior can be induced.[38–41] Bennett *et al.*[42] have shown that this behavior can be exploited to produce a rich variation in the magnetic properties as a function of depth, potentially including the generation of exotic states such as spin glasses. In the present work, we use a combination of non-destructive experimental techniques and extensive simulations to elucidate a direct correspondence between the nature and concentration of induced defects and the resulting modification of the magnetic depth profile as the irradiating fluence increases. In doing so, we show that it is possible to select values of the single-step irradiation fluence which produce technologically useful magnetic depth profiles such as flat magnetization depth-distributions, with M_s = ~1250 emu cm^{-3}, or a bilayer phase structure.

The magnetization depth profile is probed using temperature-dependent polarized neutron reflectometry (PNR). We determine the magnetic structure of four ~40 nm thick uncapped FeRh thin films on MgO substrates, each irradiated by 25 keV Ne^+ ions with fluences of 0 ions cm^{-2} (the as-grown sample), 7.5 × 10^{13} ions cm^{-2}, 3 × 10^{14} ions cm^{-2}, and 6 × 10^{14} ions cm^{-2}; these give peak atomic displacements of 0.2, 0.7, and 1.5, respectively, estimated using the Stopping and Range of Ions in Matter (SRIM) code.[43] In order to further understand the physical mechanism responsible for the modification of the magnetic properties, the PNR data are complemented by conversion electron Mössbauer spectroscopy (CEMS), Doppler broadening variable energy positron annihilation spectroscopy (DB-VEPAS), and variable-energy positron annihilation lifetime spectroscopy (VEPALS) measurements. Analysis of the irradiation-induced atomic displacements and the corresponding magnetization depth profiles provides insight into the mechanisms governing the magnetic phase transitions in the films. Crucially, by comparing the magnetic depth profiles measured by PNR to simulations conducted under the binary collision approximation, we identify that the disorder induced MPTs occur more readily at the interfaces than in the bulk of the film.

RESULTS

The in-plane thermomagnetic response of the as-grown sample was determined using vibrating sample magnetometry (VSM) over a range of temperature T = (25–200) °C under an in-plane applied field of 1 kOe, as shown in Fig. 1(a). The data demonstrate a clear hysteretic phase transition, with a peak magnetization of 1060 emu cm^{-3}. The phase transition temperature and hysteresis are determined from the peak positions of dM/dT vs temperature [see the inset of Fig. 1(a)], where M is the sample magnetization. The transition temperature T_t is determined from the peak in the heating branch, and the thermal hysteresis is quantified by the heating/cooling peak separation. This gives T_t = 73 °C with a hysteresis of 21 °C, which are typical values for well-ordered FeRh thin films.[44] Shown in Fig. 1(b) are in-plane M–H curves measured from the as-grown sample at 25 °C, 65 °C, 115 °C, and 160 °C. The data show that M_s is reached at <1 kOe at all measured temperatures. In-plane M–H curves from each irradiation condition measured at 25 °C are provided in Fig. 1(c). These data show that the samples irradiated by 7.5 × 10^{13} ions cm^{-2} and 3 × 10^{14} ions cm^{-2} produce a large magnetic response, with M_s = 1005 emu cm^{-3} and M_s = 1140 emu cm^{-3}, respectively. In contrast, the as-grown sample and the sample irradiated by 6 × 10^{14} ions cm^{-2} are only weakly magnetic at room temperature, with M_s = 35 emu cm^{-3} and M_s = 61 emu cm^{-3}, respectively.

To determine the thickness, roughness, density, and crystallinity of the as-grown FeRh films, x-ray reflectivity (XRR) and x-ray diffraction (XRD) measurements were conducted on the as-grown sample using a θ–2θ geometry. The XRR data (provided in Fig. S1 of the supplementary material, with fitting parameters in Table S1) were fitted by a dynamical simulation[45] of the reflectivity profile to determine the x-ray scattering length density (xSLD) as a function of depth. The data are modeled as a single structural layer of uniform xSLD on which a low density ~1 nm oxide layer appears to be present, as determined by an improvement to the fit. The formation of an oxide layer of this thickness is consistent with previous reports.[42,46] The fitted data indicate that FeRh has a thickness of 37 nm and a density of ρ_{FeRh} = 0.0389 f.u. Å^{-3}, which is within 6% of the bulk value.[47] The structural roughness of the substrate, FeRh, and native oxide layers are all less than 2 nm. Peak intensities measured using XRD show that the order parameter, S, is close to 0.82, corresponding to a high degree of B2 ordering (see Fig. S2 of the supplementary material).

To determine the depth-dependent relationship between ion irradiation fluence and in-plane magnetization, spin up (R^+) and spin down (R^-) neutron reflectivities were collected over a range of scattering vectors 0 Å^{-1} ≤ Q ≤ 0.1 Å^{-1} from each of the irradiated samples at 25 °C, 65 °C, 115 °C, and 160 °C [Figs. 2(b)–2(d)]. Data were also collected from the as-grown sample at 25 °C and 160 °C [Fig. 2(a)] to provide high contrast in the magnetic behavior, as determined from the magnetometry data [Fig. 1(a)]. All measurements were undertaken with an in-plane applied field of 1 kOe to ensure saturation of the sample [Fig. 1(b)], allowing the magnetization as a function of depth to be effectively modeled by a series of

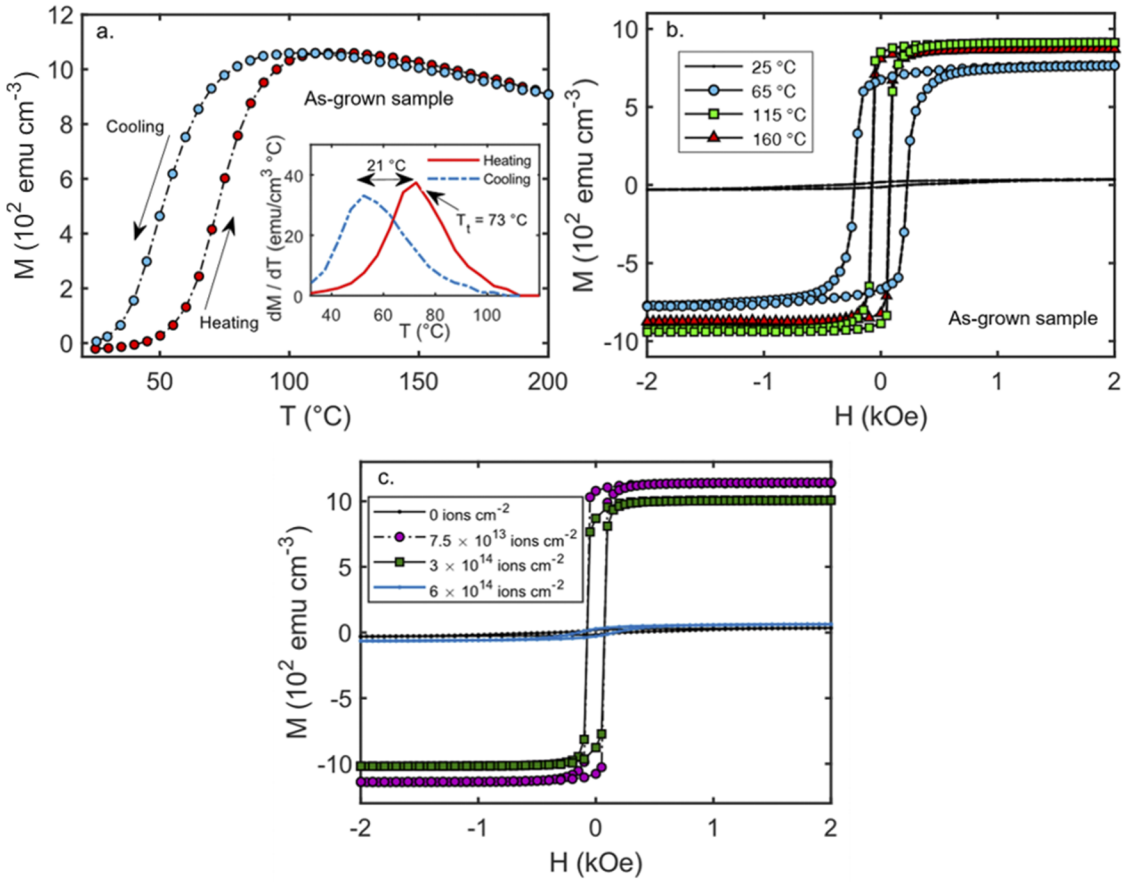

FIG. 1. (a) Temperature-dependent magnetization measurements under a 1 kOe in-plane applied field for the as-grown film. FeRh undergoes a clear MPT to FM ordering, with a transition temperature of 73 °C and a hysteresis width of 21 °C, as shown by the plot of d*M*/d*T* against *T* (inset). (b) In-plane *M*–*H* curves for the as-grown film at 25 °C, 65 °C, 115 °C, and 160 °C. (c) In plane *M*–*H* curves measured for each sample at 25 °C.

fully polarized macrospin layers. The parameters used to fit the PNR data are provided in Table S2 of the supplementary material.

To avoid overfitting, initial modeling of the PNR data followed the assumption that each sample comprised a single FeRh layer with no structural or magnetic gradients. In all cases except for the 7.5 × 10^{13} ions cm^{-2} irradiated sample, this proved insufficient to describe the reflectivity profiles, producing reduced $\chi^2 \gg 1$. Hence, additional layers were iteratively introduced to the model until the reduced χ^2 reached an asymptotic value, at which point no further parameters were included (see Fig. S3 of the supplementary material).

Figures 3(a)–3(d) show the nuclear (nSLD) and magnetic (mSLD) scattering length densities as a function of depth for all measured films. Here, the nSLDs are shaded gray, while the mSLDs are shaded blue, purple, red, and green for the 25 °C, 65 °C, 115 °C, and 160 °C cases, respectively. The nSLD profiles show that for all samples, the density of scattering centers is approximately uniform throughout the depth of the FeRh film, with a nSLD of ~5.35 × 10^{-6} $Å^{-2}$. Consequently, the magnetic scattering length density (mSLD) profiles [colored areas in Figs. 3(a)–3(d)] can be interpreted as being directly proportional to the in-plane magnetization, with a shared proportionality across the range of irradiation conditions.

By integrating the mSLD profiles over the film depth, it is possible to compare total in-plane magnetization values to those measured by VSM, as shown in Fig. 3(e). The VSM and PNR measurements are in good agreement, demonstrating that as temperature increases, the magnetization of the as-grown sample approaches that of the sample irradiated by 7.5 × 10^{13} ions cm^{-2}, while the sample irradiated by 3 × 10^{14} ions cm^{-2} features a reduced M_s compared to the lowest fluence case across the full range of measured temperatures. The small discrepancies between the total magnetizations at 160 °C as measured by PNR and those measured by VSM are likely a consequence of imperfect thermalization of the sample during PNR measurement.

To investigate how the depth-dependent magnetization profiles are correlated with the local atomic environment of ^{57}Fe, zero-field conversion electron Mössbauer spectroscopy (CEMS) measurements were performed on each sample at room temperature using

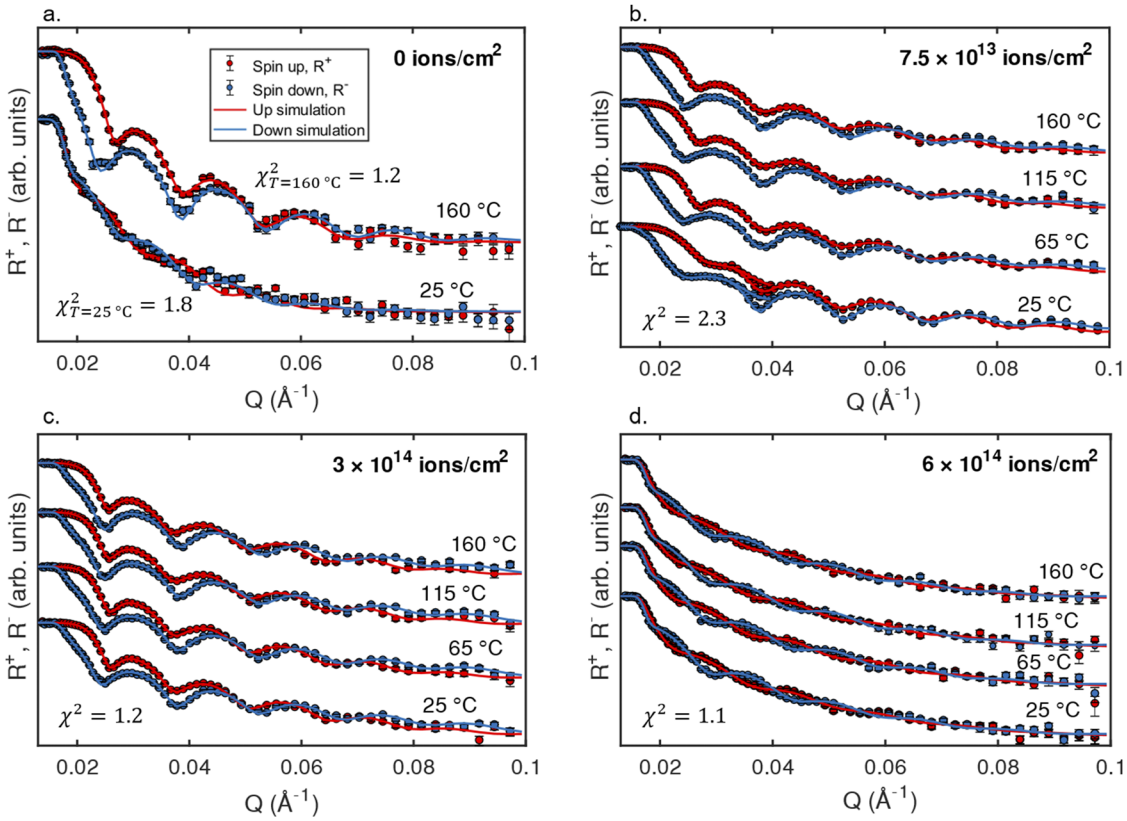

FIG. 2. (a) Measured spin up (R^+, red data) and spin down (R^-, blue data) reflectivities as a function of Q from the as-grown sample at 25 °C and 160 °C, with corresponding fitted simulations (solid lines) and χ^2 values. [(b)–(d)] Data and fits for each irradiated sample at 25 °C, 65 °C, 115 °C, and 160 °C. In all cases, the data and fits have been arbitrarily rescaled by a multiplicative constant in order to aid legibility.

a ^{57}Co source in a Rh matrix. Measurements of the intensities and positions of resonant absorption peaks due to the hyperfine field allow the local charge density, nuclear magnetic moments, and relative coexistence of AF, FM, and PM phases to be determined with high resolution. The spectra from each sample are shown in Fig. 4, which include least-squares fits comprising weighted AF, FM, and PM spectral contributions.

The as-grown sample shows a predominantly magnetic sextet sub-spectrum with a hyperfine splitting of 254 kG correlating with AF B2-FeRh (green line) and a small singlet contribution from the PM fcc phase (purple line). The hyperfine field for the as-grown state is in good agreement with previously reported values,[29] while in the present case, the spin alignment in the AF phase is only partially in-plane oriented with an average angle of 66° between spin and film normal, similar to Ref. 48. On irradiating with 7.5×10^{13} ions cm^{-2}, the hyperfine splitting increases to 271 kG, which demonstrates that the FM B2 phase (orange line) becomes the dominant contribution, with nearly zero AF contribution. Increasing the ion fluence to 3×10^{14} ions cm^{-2} results in the FM B2 phase remaining in the dominant contribution, but PM fcc-FeRh begins to become significant, and any remnants of AF B2-FeRh are fully quenched. Finally, at an irradiation fluence of 6×10^{14} ions cm^{-2}, the sextet collapses into a single resonance, denoting that the film has transitioned into the PM fcc phase.

Modeling the CEMS data provides additional information, and the parameters obtained are given in Table I. The integrated intensities of the AF, FM, and PM peaks provide a measure of their relative abundances (A_{AF}, A_{FM}, and A_{PM}) for each ion irradiation fluence under the assumption that ^{57}Fe atoms are evenly distributed throughout the samples.[49] Here, $\langle B_{hf} \rangle$ and $\langle \delta_{iso} \rangle$ are the average hyperfine field and average isomer shift of the AF and FM phases. The data confirm that the 7.5×10^{13} ions cm^{-2} irradiated sample is primarily comprised of the FM phase, with a small PM contribution of ~5%. Furthermore, the 3×10^{14} ions cm^{-2} irradiated sample consists of ~88% FM B2-FeRh and ~12% PM fcc-FeRh. At 6×10^{14} ions cm^{-2} fluence, there is no evidence of any magnetically ordered FeRh phases.

For each of the CEMS spectra, any displacement of the line of symmetry that bisects the sextet from the zero-velocity position, the isomer shift, can be attributed to differences in the density of s-orbital electrons of ^{57}Fe with respect to those of the ^{57}Co source. For the data shown in Fig. 4, the AF and FM peak isomer shifts are not equivalent. Therefore, we concentrate on the average isomer shift $\langle \delta_{iso} \rangle$ for both magnetically ordered phases and observe

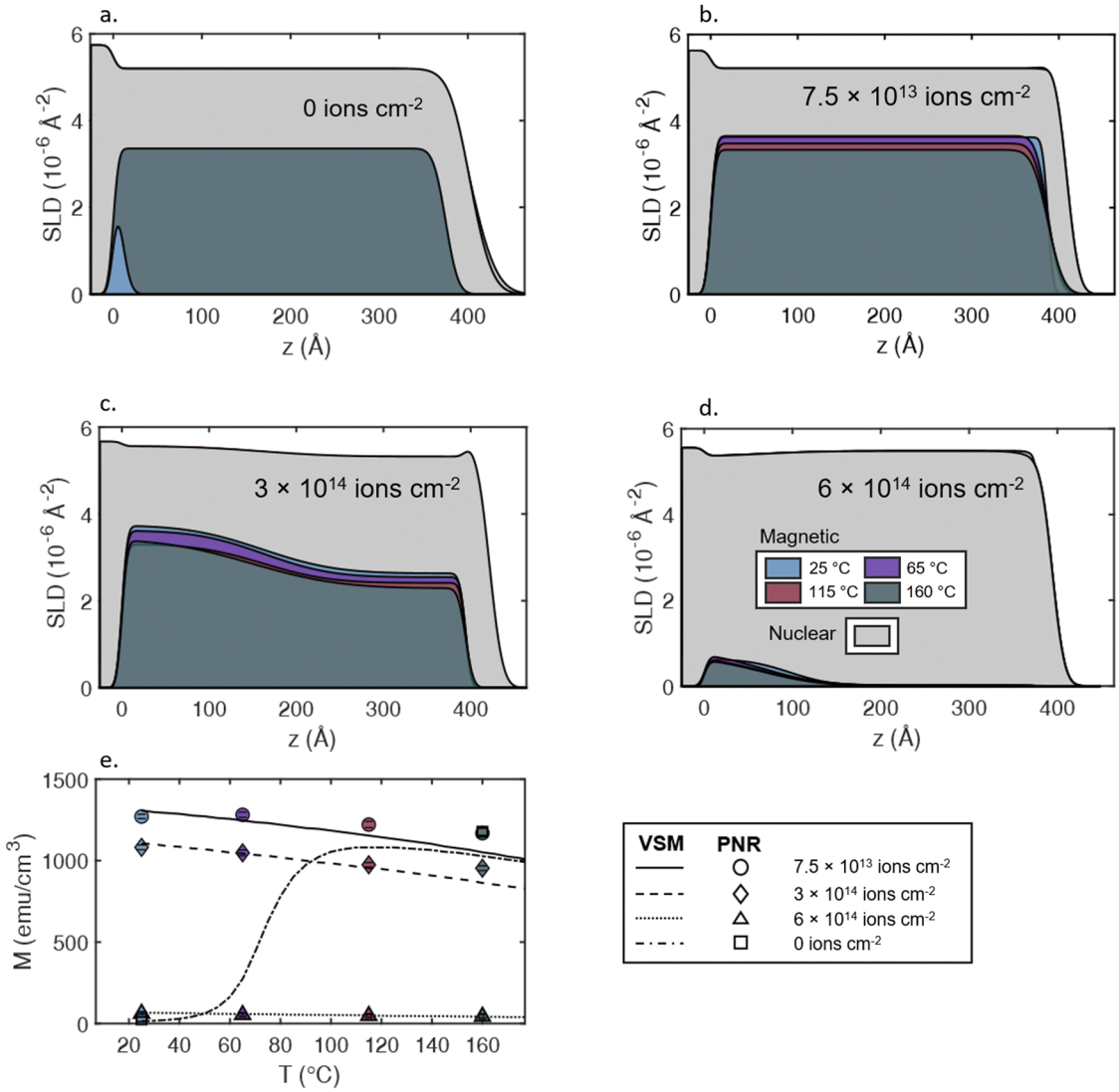

FIG. 3. [(a)–(d)] Magnetic and nuclear scattering length density (mSLD and nSLD) profiles corresponding to the fitted PNR data for each sample across the range of measured temperatures. Here, the gray areas are the nSLDs, and colored areas are the mSLDs. (e) The total in-plane magnetization as measured by PNR (symbols) and VSM (lines) demonstrates good agreement between the two methods.

an increase with a rise in fluence. The increase in the isomer shift is explained by the lattice expansion, which has been shown to occur with the disorder induced MPT,[40] similar to the temperature induced case.[50]

To understand the nature of the structural modifications induced by the ion irradiation, which leads to the changes in magnetic properties, we conducted an *in situ* analysis of ion-induced defect formation using Doppler broadening variable energy positron annihilation spectroscopy (DB-VEPAS). Here, the line broadening of gamma photons resulting from positron annihilation is characterized by two parameters, S and W, which represent positrons annihilating with low momentum valence electrons (sensitive to vacancy type defects and their concentration) and with high momentum core electrons, respectively. The S-parameter as a function of positron implantation energy E_P and mean implantation depth $\langle z \rangle$ for all samples is shown in Fig. 5(a). The approximate position of the film/substrate interface is marked as a dotted line. The depth profiles of the S-parameter exhibit typical slow decaying behavior for systems with a relatively small defect concentration. The smooth changes in slope at the interface indicate good crystallinity.

In order to estimate relative changes in defect concentration, analysis of the positron diffusion length, L_+, and specific S-parameters has been conducted by fitting the $S(E_P)$ curves using the VEPFit code.[51] In general, L_+ is inversely proportional to defect

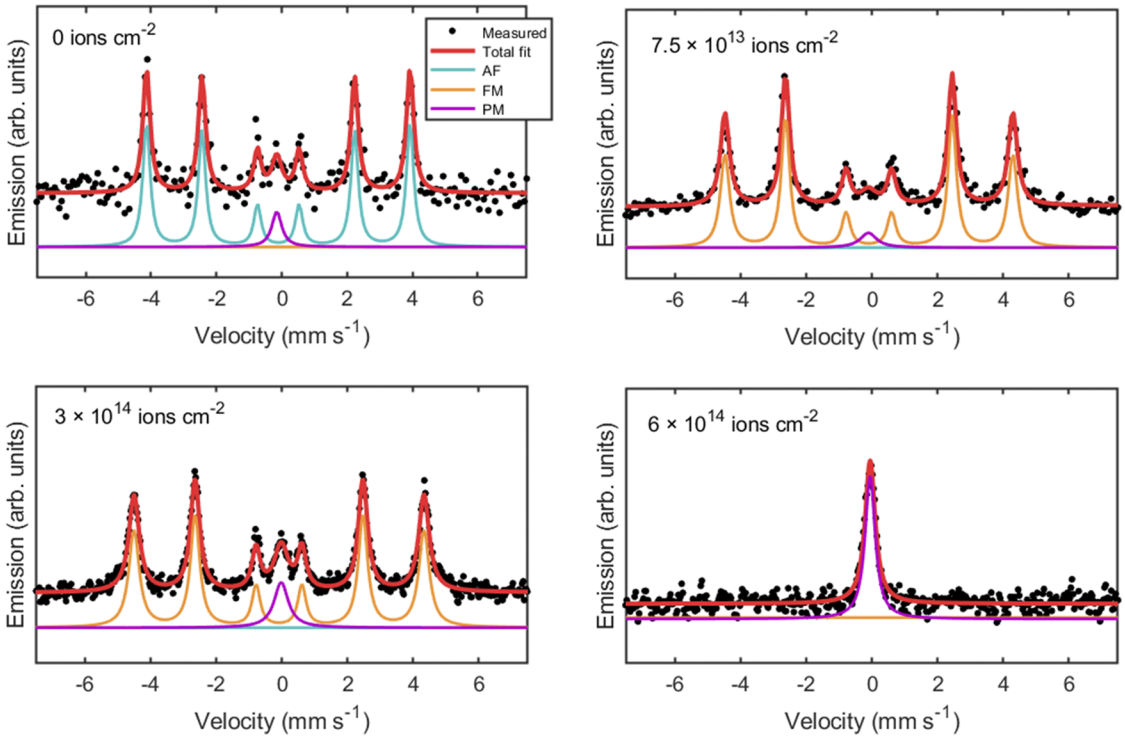

FIG. 4. CEMS data and corresponding fits for each irradiation fluence. Each fit comprises a weighted sum of contributions from AF, FM, and PM phases, which are also shown.

concentration. The calculated L_+ with corresponding defected layer thicknesses is given in Table II. Ion irradiation of FeRh produces vacancy-like defects, which is particularly evident for the two largest fluences where the diffusion length drops by roughly a half, demonstrating that the defect concentration is concomitantly increased. For the 7.5×10^{13} ions cm^{-2} sample, the $S(E_P)$ dependence shows an additional maximum close to the substrate interface, which can be attributed to defect clusters.[52] In order to model this, a bilayer system has been assumed, where a thin region of larger defect concentration ranging from 32 nm to 40 nm, which is 8 nm closest to the MgO substrate, is given by the calculations (Table II).

The sensitivity of the positron lifetime to the local electron density was also exploited using variable energy positron annihilation lifetime spectroscopy (VEPALS). The electron density is reduced in vacancy-like defects, and the resulting positron lifetime is proportional to the defect size. Two prominent lifetimes have been found for all the samples, which will be referred to as τ_1 and τ_2, where $\tau_1 \approx$ (150–190) ps and $\tau_2 \approx$ (250–400) ps. Theoretical calculations of positron lifetimes in the case of B2 and fcc FeRh phases for the delocalized states (i.e., the bulk lifetime) and the localized trapped states at defects were obtained by using an atomic superposition (ATSUP) approach using two-component density functional theory (DFT) *ab initio* calculations.[53] For the electron–positron correlation, the generalized gradient approximation (GGA) scheme was used.[54] According to our DFT calculations and existing literature,[55] τ_1 can be ascribed to a Rh (calculated lifetime: ~186 ps) or Fe (~177 ps) monovacancy (V_{Rh} or V_{Fe}) for the as-grown state. The variation of τ_1 with implantation energy is provided in Fig. 5(b) for each

TABLE I. Fitted parameters obtained from the experimental spectra shown in Fig. 4. Values marked with an asterisk were fixed during the fitting procedure. Numbers in brackets denote uncertainties in the trailing digit/s.

Fluence (ions cm^{-2})	A_{AF} (%)	A_{FM} (%)	A_{PM} (%)	$\langle B_{hf} \rangle$ (kG)	$\langle \delta_{iso} \rangle$ (mm s^{-1})
0	91.9(2.3)	0*	7.9(2.3)	254(1)	0.006(1)
7.5×10^{13}	6.1(9)	88.8(6)	5.1(7)	271(3)	0.016(2)
3×10^{14}	0*	87.7(5)	12.3(5)	274(1)	0.024(2)
6×10^{14}	0*	0*	100*	0*	0*

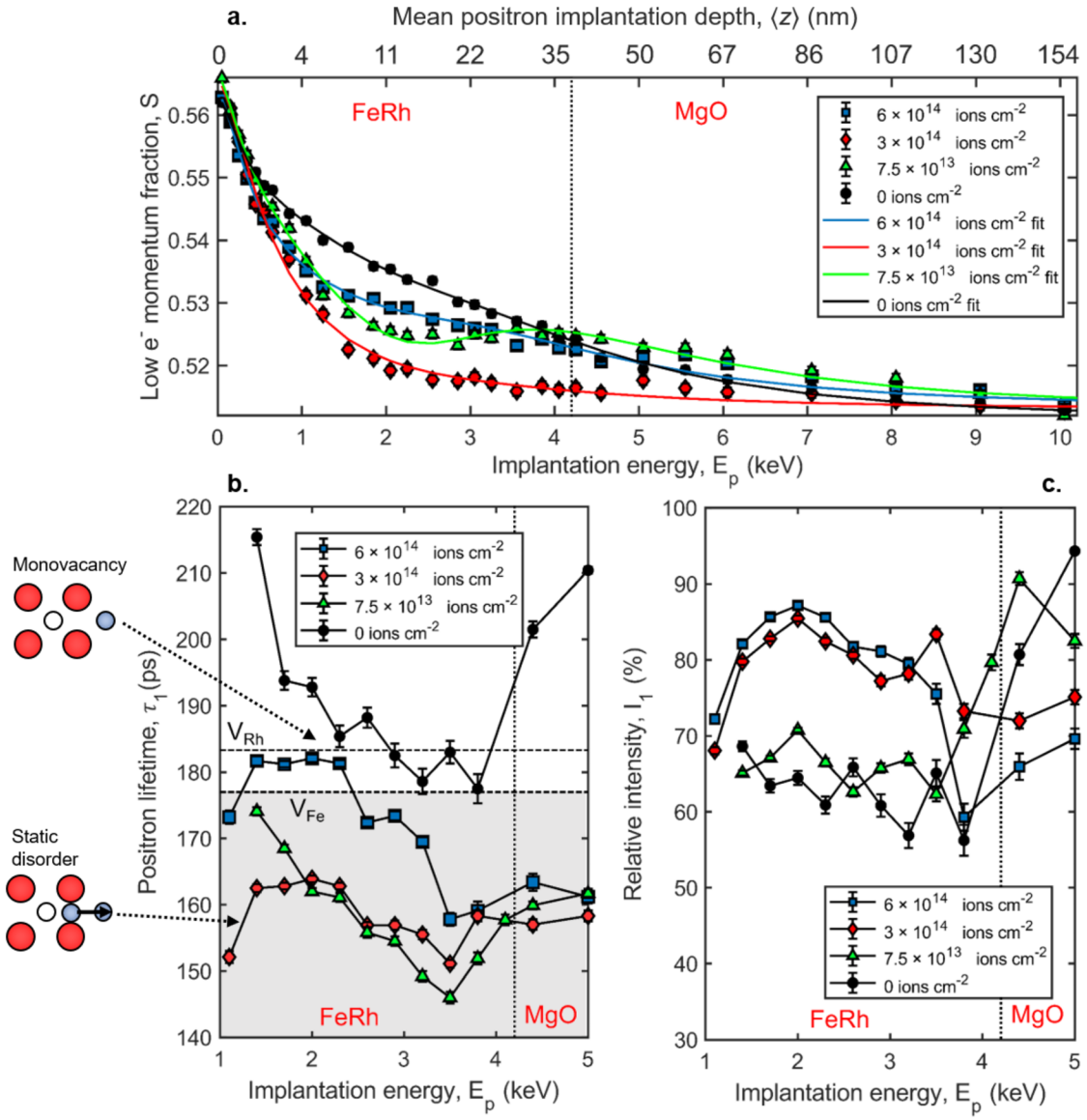

FIG. 5. (a) The *S*-parameter as a function of positron implantation energy E_p and mean implantation depth $\langle z \rangle$ for the as-grown and irradiated samples with different ion fluences. Also provided are fits to the data (VEPfit code), as shown by the solid lines, which enable calculation of the positron diffusion length L_+. [(b) and (c)] The positron lifetime component τ_1 and its intensity I_1 as a function of positron implantation energy E_p are given, respectively. Horizontal lines indicate a DFT calculated lifetime of single Fe and Rh vacancies. Vertical dotted line marks the approximate position of the substrate interface.

fluence condition. The calculated value for delocalized bulk annihilation is 103 ps, which has not been observed, suggesting a substantial initial defect concentration. For the 7.5×10^{13} ions cm^{-2} and 3×10^{14} ions cm^{-2} cases, τ_1 is smaller than the calculated values for monovacancies and larger than the bulk lifetime, which is an indication for the occurrence of dislocations[56] or equivalent open volumes. A schematic description of the relationship between positron lifetime and atomic displacement is shown in Fig. S4 of the supplementary material, where depending on the dislocated atom position, the lifetime varies between that of the bulk and of a monovacancy. The depth profile of the largest fluence sample shows a large variation of lifetime, with greater lifetime values in the top half of the film region, representing V_{Fe}, and smaller lifetimes closer to the substrate interface, indicating some remaining static disorder. The longer lifetime component τ_2 likely represents the superposition of vacancy clusters at crystallites boundaries and at surface states for positrons back-diffused to the surface due to relatively long L_+ (Table II).

TABLE II. Layer thicknesses and positron diffusion lengths from fits to S(EP) curves. Parameters were calculated using the VEPFit code. The numbers in brackets denote uncertainties in the trailing digit/s.

Fluence (ions cm^{-2})	Thickness 1 (nm)	$L_{+,1}$ (nm)	Thickness 2 (nm)	$L_{+,2}$ (nm)
0	40.0	10.74(5)	...	...
7.5×10^{13}	32.4(3)	10.13(4)	7.6(3)	8.6(2)
3×10^{14}	40.0	4.96(3)	...	...
6×10^{14}	40.0	5.48(4)	...	...

The variation of the relative intensity I_1 [Fig. 5(c)] represents an increase in defect concentration as fluence increases. This increase is only slight for the lowest fluence but is more significant for the two highest fluences, corroborating the trend in the L_+ values of Table II and hence confirming that the overall defect concentration increases with an increase in fluence. The relative intensity is proportional to defect concentration, provided that the positron trapping rate remains similar. Here, the trapping rate should decrease due to the shorter positron lifetime,[57] which confirms the origin of the changes to I_1 as being due to an increasing defect concentration. In addition, the depth profile of I_1 is largely constant, which indicates dominant trapping in defects with limited back-diffusion to the surface. Moreover, it validates that the lifetime variations across the film thickness are due to variations of the defect microstructure and not a consequence of signals' superposition from the surface and substrate.

DISCUSSION

We have previously reported temperature-dependent PNR results from uncapped FeRh films of several thicknesses, where we showed that in the nominally AF phase, a non-zero magnetization occurs in the region of the FeRh film closest to the substrate.[58] This effect is observed here in the as-grown case; see Fig. 3(a). The interfacial moment has been variously ascribed to the epitaxial strain from the slight lattice mismatch between FeRh and MgO,[59] coexistence of the α' and γ phases during the initial stages of growth,[60] and Fe- or Rh-rich regions.[46,58,61] Although we make no assessment regarding the origin of the interfacial FM observed here, we note that the PNR fit is not improved by the inclusion of a similar effect at the FeRh/ambient interface. The data demonstrate that upon heating, the as-grown film undergoes the MPT transition uniformly through the film depth, reaching an mSLD of 3.7×10^{-6} $Å^{-2}$ (equivalent to 1177 emu cm^{-3}) at 160 °C. The VEPALS analysis strongly indicates the existence of monovacancies in the as-grown film. The calculated values for Fe and Rh monovacancies in the B2 phase are very close to each other and hence are difficult to separate experimentally, but the lifetime value from the interface region corresponds most closely to V_{Fe}.

Upon irradiating with 7.5×10^{13} ions cm^{-2}, static disorder is induced, while the long range B2 structure is retained. The PNR data are effectively modeled by a single structural layer of uniform in-plane magnetization, which is stable over the entire range of measured temperatures, diminishing only slightly with an increase in the temperature. This can be seen in the mSLD, shown in Fig. 3(b), which has the same constant value of 3.7×10^{-6} $Å^{-2}$ (1177 emu cm^{-3}) throughout the film at 25 °C, indicating that the FM phase has been induced to the maximum degree. At this fluence, the reduced positron lifetime suggests that the monovacancies are suppressed by the ion bombardment and are replaced by smaller open-volume defects such as dislocations, as evidenced by the reduced positron lifetime compared to the as-grown case [Fig. 5(b)]. This defect state is consistent with static disorder, which has been recently shown to be associated with the occurrence of the FM state.[29] At the same time, the positron diffusion length L_+ is essentially unaffected across the whole film thickness apart from the interface region, where a slight decrease is observed (see Table II). The relative intensity I_1 remains unchanged compared to the as-grown state, showing a sharp increase in the interface region [Fig. 5(c)]. Thus, the overall defect concentration does not change, but the defect type is clearly different after irradiation.

Increasing the fluence to 3×10^{14} ions cm^{-2} raises the concentration of static disorder not only at the interface but also across the entire thickness of the film, as shown by the decrease in L_+ and increase in I_1. The PNR data at this fluence are well-described using a bilayer model where FeRh is divided into two sublayers with approximately uniform density but with different in-plane magnetizations [Fig. 3(c)]. The result is an mSLD at 25 °C, which is 3.7×10^{-6} $Å^{-2}$ (1177 emu cm^{-3}) in the region closest to the substrate, compared to 2.6×10^{-6} $Å^{-2}$ (923 emu cm^{-3}) at the top surface of the film. On heating, the mSLD profile does not undergo any significant change in the shape but does reduce slightly in magnitude throughout the film depth, with the 160 °C mSLD reduced by 6% compared to the 25 °C mSLD. The fact that the mSLD does not change the shape with an increase in the temperature provides evidence that the suppression of the magnetization toward the top surface of the film is due to the formation of the PM fcc phase, rather than any remaining AF B2 phase.

On increasing the irradiating fluence to 6×10^{14} ions cm^{-2}, the FeRh layer becomes almost entirely PM, featuring a region of only slight FM ordering in close proximity to the MgO, which is approximately constant with an increase in the temperature [Fig. 3(d)]. This region, which extends ~14 nm from the substrate interface, has a maximum mSLD of 6.7×10^{-7} $Å^{-2}$ (119 emu cm^{-3}) at 25 °C, which gives an average magnetization for the entire film of 64 emu cm^{-3}, in agreement with the bulk magnetometry. The defect microstructure for this sample is defined by the ion damage profile, where at the position of maximum damage (E_P = 2 keV, $\langle z \rangle \approx$ 11 nm, dpa = 1.45), a larger number of small single vacancies are generated, whereas closer to the substrate interface (a smaller damage of dpa = 0.2), a signature of static disorder remains.

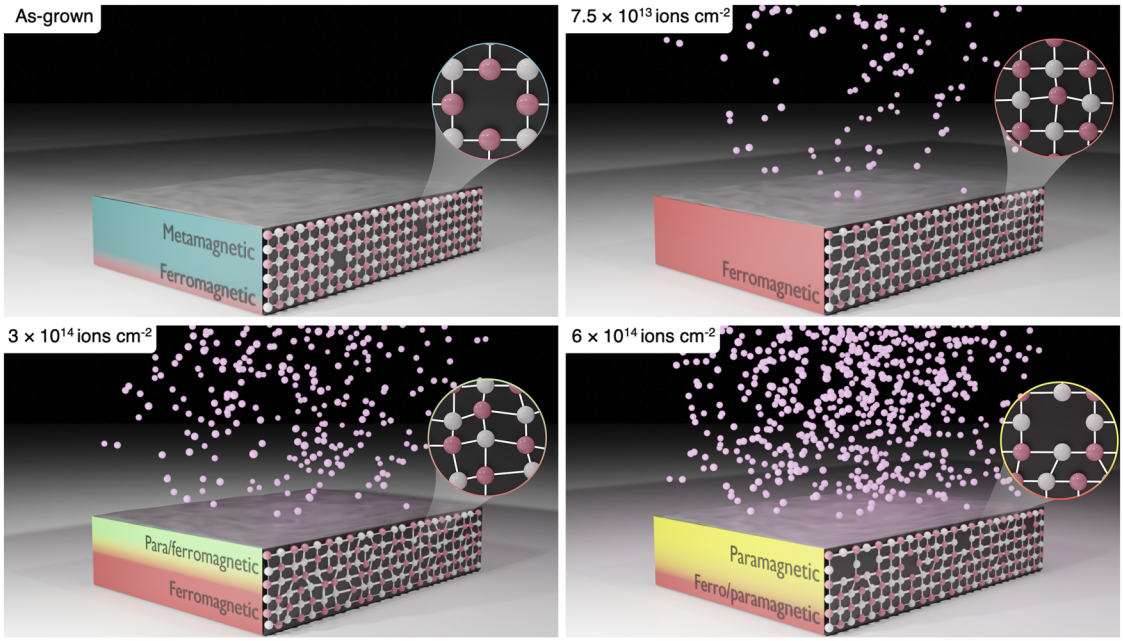

FIG. 6. As the irradiation fluence increases, the metamagnetic FeRh first becomes uniformly FM through the film depth and then transitions to a bilayer structure where the layer closest to the substrate is maximally FM, while the topmost layer of the film features a mixture of FM and PM phases. At the maximum fluence, the film becomes almost entirely PM, with a layer of residual FM at the interface. The dominant defect type is also shown for each case.

The PNR, CEMS, and positron data allow the effect of increasing fluence ion irradiation to be explained, as shown schematically in Fig. 6, wherein the onset of FM and PM behaviors is associated with the emergence of static disorder and monovacancy defects, respectively. As a result of the ion damage, the depth-dependent magnetic phase profile is either uniform or can be described by a simple bilayer configuration.

The magnetization depth profiles can be modeled by considering the interaction of the Ne^+ ions with the FeRh film. Simulations performed by applying a binary collision approximation (SRIM)[43] show a typical quasi-Gaussian distribution of the atomic displacements with the film depth (Fig. S5 of the supplementary material). Comparing the simulated depth variation of atomic displacements with observed magnetization depth distributions provides further insight into the relationship between magnetization and atomic scale defects. For instance, the flat M_s-distribution of the 7.5×10^{13} ions cm^{-2} case, when compared analytically to its inhomogeneously distributed atomic displacements, reveals that 1 displacement every 37 atoms may be sufficient to induce 99% of M_s of the FM phase. This is consistent with recent observations that show the AF to FM transition in FeRh originating from small displacements of the Fe and Rh atoms from their equilibrium positions,[29] rather than via antisites. A comparison of the PNR-observed M_s-distribution to the simulated displacements can also be performed for the higher fluence samples, where the transition to the fcc structure occurs. This is a less sensitive transition, wherein it can be shown that ~1 displacement for every atom is required on average for a 50% reduction of M_s. The structural phase transition also appears to be influenced by interfacial effects, where generally an M_s suppression is expected.[11,58,62] Using a semi-empirical approach [Eq. (S2) of the supplementary material] reveals that the form of the depth-dependent magnetization observed by PNR for the FM to PM transition in the two highest fluence cases can be understood in terms of magnetization suppression at the surface, in addition to the decay due to the increasing atomic displacements.

CONCLUSIONS

We have demonstrated that it is possible to exploit irradiation-induced disorder to generate phase transitions in single layer FeRh films, allowing the magnetic properties to be tailored. The magnetic phases (AF, FM, or PM) occurring within the thin film can be manipulated with depth selectivity so as to achieve a homogeneously magnetized FM layer or to realize interfaces between regions of different magnetic phase distributions, a desirable property for spintronic applications where the relative coexistence of the various phases is critical. We have shown that the disorder induced MPT from AF to FM ordering is driven by static disordering, while the FM to PM transition is coupled to the appearance of monovacancy defects. Furthermore, we have found evidence that the disorder induced transition to fcc PM-FeRh tends to nucleate more readily in the regions close to the ambient interface, whereas a similar effect is observed in the thermally driven MPT at the substrate interface.

For all samples, our data are well described assuming AF, FM, and PM phases only and do not present evidence for exotic states such as spin glasses or magnetic dead layers. This feature, coupled to the fact that the mSLD profiles of the irradiated samples comprise relatively few sublayers with discrete magnetizations that are stable with respect to increasing temperature, highlights the effectiveness of sensitive and controlled disordering of ordered alloy precursors for producing technologically useful magnetic configurations. Our results provide the basis for the patterning of single layer or multilayer structures that incorporate FeRh to create devices on sub-100 nm length scales with AF and FM order in close physical proximity.

EXPERIMENTAL

Fabrication and ion irradiation

FeRh films with 40 nm nominal thickness were grown onto commercial (001)-oriented single crystal MgO substrates by dc magnetron sputtering from a 2-in. stoichiometric $Fe_{50}Rh_{50}$ target using 100 W power and 3 mTorr working pressure and a base pressure of $\sim 10^{-8}$ Torr. The substrates were baked *in vacuo* at 650 °C for 2 h prior to growth, and this temperature was maintained throughout the deposition. The films were subsequently annealed at 750 °C for 2 h and then cooled to room temperature in the sputtering chamber for 4 h.

For ion irradiation, Ne^+ ions were accelerated onto the $Fe_{50}Rh_{50}$ thin films in vacuum (2×10^{-6} mbar) using a 40 Ne^+ kV low-energy ion implanter 1090-50 (Danfysik A/S, Taastrup, Denmark). The ion-beam, which was ~10 mm in diameter, was rastered over the sample at a rate of 1 kHz. A fluence of 7.5×10^{13} ions cm^{-2} was deposited in 4 min using a beam current of 60 nA cm^{-2}. The samples remained at room temperature during the irradiation process, for fluences of up to 6×10^{14} ions cm^{-2} deposited in 11 min at a beam current of 155 nA cm^{-2}.

Preliminary characterization

X-ray reflectivity (XRR) and x-ray diffraction (XRD) measurements were conducted using a Rigaku SmartLab x-ray diffractometer equipped with a D/teX Ultra 250 silicon strip detector and a two-bounce Ge(220) monochromator. This instrument generates x rays at the $CuK_{\alpha 1}$ edge ($\lambda = 1.541$ Å). Measurements were performed using a step size of $2\theta = 0.01°$. Structural layer thicknesses, densities, and roughnesses were obtained by fitting a dynamical simulation to the XRR data using the GenX reflectivity package,[45] which uses a combined simplex/differential evolution genetic algorithm to optimize a model of the xSLD profile. Thermomagnetic measurements were performed before and after ion irradiation using a MicroSense Model 10 vibrating sample magnetometer (VSM) across a temperature range of (25–200) °C under an in-plane applied field of 1 kOe. Normalization by the sample volume was conducted using the film thickness as determined by fits to the XRR data. Prior to VSM measurement, the sample was de-ionized to preclude the erroneous signal from electrostatic build-up. Background correction was done by measuring and subtracting the diamagnetic response of a blank MgO substrate over the same temperature range under the same applied field. M–H curves were measured using the same apparatus. Here, background correction was achieved by a linear fit to the diamagnetic response.

Polarized neutron reflectometry

PNR measurements were made on the POLREF instrument at the ISIS Neutron and Muon Source at the Rutherford Appleton Laboratory. Samples were cleaned with acetone and isopropanol in an ultrasonic bath and then mounted on a copper stage with thermally conductive paste. The puck was placed into a vacuum furnace at a pressure of 5.5×10^{-7} mbar situated in a uniform 1 kOe magnetic field. Spin resolved neutron reflectivities were then obtained at each temperature setpoint (increasing), with the system left to thermalize for 2 h prior to measurement at each temperature. An incident angle of $\theta = 0.9°$ was used, which provides a range in Q of (0.014 –0.993) $Å^{-1}$. For the 7.5×10^{13} ions cm^{-2} irradiated sample at 25 °C, incident angles of $\theta = 0.4°$ and $\theta = 1.4°$ were used, leading to a range in Q of (0.081–0.148) $Å^{-1}$. Here, resolution is dominated by the sample, resulting in a strong θ-dependence, and hence, the data feature a notable discontinuity at ~0.04 $Å^{-1}$. For this reason, the data from this measurement were not stitched but were instead fitted with separate resolution functions.

The PNR data were fitted to dynamical simulations of spin-resolved neutron reflectivities using the GenX reflectivity package.[45] For each sample, all data across the range of measured temperatures were fitted simultaneously using a shared reduced χ^2 figure of merit, effectively quadrupling the number of data points that contribute to the fitted value of each structural parameter. Layer magnetizations, layer roughnesses, and incident beam intensities were allowed to vary between temperature measurements. Maximum and minimum values for the layer thicknesses, densities, and roughnesses were informed by the values determined from XRR.

Conversion electron Mössbauer spectroscopy

^{57}Fe Mössbauer spectroscopy in zero external field at perpendicular incidence of the γ rays to the film surface was performed by detection of conversion electrons (CEMS). For the detection of the electrons, the sample was installed in a proportional gas counter, i.e., a housing with a continuous He gas flow mixed with 4% CH_4 to avoid ionization processes. For the measurement, a constant acceleration Mössbauer driving unit was used with a ^{57}Co source embedded in a Rh matrix, while the velocity of the spectrometer was calibrated with an α-Fe foil reference sample at room temperature. The experimental spectra were evaluated by a least-squares fitting routine using the PI program package.[63] The discussed isomer shifts δ_{iso} are given relative to bulk bcc Fe at room temperature.

Doppler broadening variable energy positron annihilation spectroscopy (DB-VEPAS)

DB-VEPAS measurements were conducted at the apparatus for the *in situ* defect analysis (AIDA)[64] of the slow positron beamline (SPONSOR)[65] at Helmholtz-Zentrum Dresden-Rossendorf. Positrons emitted from a radioactive ^{22}Na source are moderated, magnetically guided, and post-accelerated to a discrete kinetic energy value E_p. When implanted into a solid, they either annihilate in delocalized lattice sites, emitting at least two 511 keV gamma

photons, or localize in open volumes, i.e., at defects or interfaces. Increasing E_p in the range of 40 eV to 35 keV enables depth profiling starting at the film surface down to a few micrometers. A mean positron implantation depth, $\langle z \rangle$, can be estimated by using a simple material density dependent formula,

$$z = (36/\rho_{FeRh})E_P^{1.6}, \quad (1)$$

where $\rho_{FeRh} = 9.76$ g cm^{-3} is the density of FeRh, $\langle z \rangle$ is in nm, and E_p is in keV. Positron–electron annihilation events are measured typically with one or two high-purity Ge detectors [an energy resolution of (1.09 ± 0.01) keV at 511 keV for a single detector configuration]. The Doppler broadening of the annihilation line is characterized by two distinct parameters, S and W, which are defined as the fraction of the annihilation line in the middle [(511 ± 0.93) keV] and outer [(508.56 ± 0.35) keV and (513.44 ± 0.35) keV] regions of the spectrum, respectively. $S(E_P)$ curves were fitted using the VEPFit code[51] to obtain values for the positron diffusion length L_+ and layer-specific S-parameters. For cases where a single layer was assumed, the thickness of the film was fixed to 40 nm. Material densities for FeRh and MgO were $\rho_{FeRh} = 9.76$ g cm^{-3} and $\rho_{MgO} = 3.6$ g cm^{-3}. For MgO, L_+ was fixed to 35 nm for all the samples, a value obtained from unconstrained fits with a deviation of ±5 nm.

Variable energy positron annihilation lifetime spectroscopy (VEPALS)

VEPALS measurements were conducted at the Mono-energetic Positron Source (MePS) beamline at HZDR in Germany, which is the end station of the radiation source ELBE (Electron Linac for beams with high Brilliance and low Emittance).[55] The typical lifetime spectrum $N(t)$ is described by $N(t) = \Sigma(1/\tau_i)\ I_i\ \exp(-t/\tau_i)$, where τ_i and I_i are the positron lifetime and intensity of the i-th component, respectively ($\Sigma I_i = 1$). All the spectra were deconvoluted using the non-linear least-squared based software package PALSfit[66] in several discrete lifetime components. In general, positron lifetime is directly proportional to defect size, i.e., the larger is the defect, the lower is the probability and the longer it takes for positrons to be annihilated with electrons.[57,67,68] The corresponding relative intensities reflect the concentration of each defect type (size). The positron annihilation lifetime and intensity were probed as a function of implantation energy E_p, which is directly related to implantation depth $\langle z \rangle$.

A digital lifetime $CrBr_3$ scintillator detector of 51 mm diameter (2 in.) and 25.4 mm length (1 in.) was used, coupled to a Hamamatsu R13089-100 PMT with a μ-metal shield and housed inside a solid Au casing. A homemade software was used, employing SPDevices ADQ14DC-2X with 14-bit vertical resolution and 2 GS/s horizontal resolution and with a time resolution function down to about 0.205 ns. The resolution function required for the spectrum analysis uses two Gaussian functions with distinct intensities depending on the positron implantation energy, E_p, and appropriate relative shifts. All spectra contained at least 1×10^7 counts.

SUPPLEMENTARY MATERIAL

X-ray measurements (XRD/R) for structural characterization, PNR fitting parameters and the corresponding reduced χ^2 values, positron lifetime values calculated using DFT, and SRIM simulations of irradiation-induced disordering are provided in the supplementary material.

ACKNOWLEDGMENTS

The authors wish to gratefully acknowledge the contribution of the x-ray characterization facilities of the Henry Royce Institute through EPSRC Grant Nos. EP/S019367/1 and EP/P025021/1. Experiments at the ISIS Neutron and Muon Source were supported by a beamtime allocation RB1910304 from the Science and Technology Facilities Council. W. G. gratefully acknowledges funding through the EPSRC Doctoral Training Partnership. The authors would also like to acknowledge Alexander Lincoln for his contribution to the PNR data acquisition and Andy Church for the design and implementation of the PNR sample environment. Ion-irradiation experiments were performed at the Ion Beam Centre, and Positron annihilation lifetime studies were carried out at the ELBE instrument at the Helmholtz-Zentrum Dresden-Rossendorf. This work was partially supported by the Impulse-und Net-working fund of the Helmholtz Association (Grant No. FKZ VH-VI-442 Memriox) and the Helmholtz Energy Materials Characterization Platform (Grant No. 03ET7015). B.E., H.W., and R.B. acknowledge financial support from the Deutsche Forschungsgemeinschaft (DFG) under Project Nos. WE2623/14-2 and BA5656/1-2. Furthermore, B.E. and H.W. acknowledge financial support from the Deutsche Forschungsgemeinschaft (DFG) within the Collaborative Research Center/Transregio (CRC/TRR) 270 (Project-ID 405553726, project B5).

DATA AVAILABILITY

The PNR data are openly available at Ref. 69. All other data that support the findings of this study are available from the corresponding author upon reasonable request.

REFERENCES

[1] M. Fallot, "Les alliages du fer avec les métaux de la famille du platine," Ann. Phys. **11**, 291–332 (1938).
[2] E. M. Hofer and P. Cucka, "Magnetic properties of Rh-rich FeRh alloy," J. Phys. Chem. Solids **27**, 1552–1555 (1966).
[3] J. B. McKinnon *et al.*, "The antiferromagnetic-ferromagnetic transition in iron-rhodium alloys," J. Phys. C: Solid State Phys. **3**, S46 (1970).
[4] J. S. Kouvel and C. C. Hartelius, "Anomalous magnetic moments and transformations in the ordered alloy FeRh," J. Appl. Phys. **33**, 1343 (1962).
[5] S. Maat, J. Thiele, and E. E. Fullerton, "Temperature and field hysteresis of the antiferromagnetic-to-ferromagnetic phase transition in epitaxial FeRh films," Phys. Rev. B **72**, 214432 (2005).
[6] L. Lewis, C. Marrows, and S. Langridge, "Coupled magnetic, structural, and electronic phase transitions in FeRh," J. Phys. D: Appl. Phys. **49**, 323002 (2016).
[7] P. H. L. Walter, "Exchange inversion in ternary modifications of iron rhodium," J. Appl. Phys. **35**, 938–939 (1964).
[8] R. Barua, F. Jiménez-Villacorta, and L. H. Lewis, "Predicting magnetostructural trends in FeRh-based ternary systems," Appl. Phys. Lett. **103**, 102407 (2013).
[9] N. V. Baranov and E. A. Barabanova, "Electrical resistivity and magnetic phase transitions in modified FeRh compounds," J. Alloys Compd. **219**, 139–148 (1995).
[10] W. Lu, J. Fan, and B. Yan, "Microstructure and magnetic properties of FeRh thin films with Pt doping," Sci. China: Phys., Mech. Astron. **54**, 1223–1226 (2011).
[11] C. Barton *et al.*, "Substrate induced strain field in FeRh epilayers grown on single crystal MgO (001) substrates," Sci. Rep. **7**, 44397 (2017).

[12]X. Zhou *et al.*, "Magnetic surface domain imaging of uncapped epitaxial FeRh(001) thin films across the temperature-induced metamagnetic transition," AIP Adv. **6**, 015211 (2016).
[13]M. G. Loving *et al.*, "Strain-tuning of the magnetocaloric transition temperature in model FeRh films," J. Phys. D: Appl. Phys. **51**, 024003 (2017).
[14]Y. Xie *et al.*, "Electric field control of magnetic properties in FeRh/PMN-PT heterostructures," AIP Adv. **8**, 055816 (2018).
[15]I. Fina *et al.*, "Reversible and magnetically unassisted voltage-driven switching of magnetization in FeRh/PMN-PT," Appl. Phys. Lett. **113**, 152901 (2018).
[16]Z. Liu *et al.*, "Full electroresistance modulation in a mixed-phase metallic alloy," Phys. Rev. Lett. **116**, 097203 (2016).
[17]J. D. Clarkson *et al.*, "Hidden magnetic states emergent under electric field," Sci. Rep. **7**, 15460 (2017).
[18]R. O. Cherifi *et al.*, "Electric-field control of magnetic order above room temperature," Nat. Mater. **13**, 345 (2014).
[19]Y. Lee *et al.*, "Large resistivity modulation in mixed-phase metallic systems," Nat. Commun. **6**, 5959 (2015).
[20]I. Fina *et al.*, "Electric-field-adjustable time-dependent magnetoelectric response in martensitic FeRh alloy," ACS Appl. Mater. Interfaces **9**, 15577–15582 (2017).
[21]I. Fina and J. Fontcuberta, "Strain and voltage control of magnetic and electric properties of FeRh films," J. Phys. D: Appl. Phys. **53**, 023002 (2019).
[22]J. Ehrler *et al.*, "Laser-rewriteable ferromagnetism at thin-film surfaces," ACS Appl. Mater. Interfaces **10**, 15232–15239 (2018).
[23]M. Foerster *et al.*, "Local manipulation of metamagnetism by strain nanopatterning," Mater. Horiz. **7**, 2056–2062 (2020).
[24]C.-H. Lee *et al.*, "The exchange bias effect on single layer of Fe-rich FeRh thin film," Mater. Lett. **254**, 309–311 (2019).
[25]I. Gray *et al.*, "Imaging uncompensated moments and exchange-biased emergent ferromagnetism in FeRh thin films," Phys. Rev. Mater. **3**, 124407 (2019).
[26]X. Z. Chen *et al.*, "Tunneling anisotropic magnetoresistance driven by magnetic phase transition," Nat. Commun. **8**, 449 (2017).
[27]Y. Wang *et al.*, "Spin pumping during the antiferromagnetic–ferromagnetic phase transition of iron–rhodium," Nat. Commun. **11**, 275 (2020).
[28]J. Ehrler *et al.*, "Magneto-structural correlations in a systematically disordered B2 lattice," New J. Phys. **22**, 073004 (2020).
[29]B. Eggert *et al.*, "Magnetic response of FeRh to static and dynamic disorder," RSC Adv. **10**, 14386 (2020).
[30]J. Ehrler *et al.*, "The role of open-volume defects in the annihilation of antisites in a B2-ordered alloy," Acta Mater. **176**, 167–176 (2019).
[31]D. Oshima *et al.*, "Control of magnetic properties of MnGa films by Kr^+ ion irradiation for application to bit patterned media," IEEE Trans. Magn. **49**(7), 3608 (2013).
[32]D. Oshima *et al.*, "Ion irradiation-induced magnetic transition of MnGa alloy films studied by X-ray magnetic circular dichroism and low-temperature hysteresis loops," IEEE Trans. Magn. **52**(7), 1 (2016).
[33]N. Gaur *et al.*, "Lateral displacement induced disorder in $L1_0$-FePt nanostructures by ion-implantation," Sci. Rep. **3**, 1907 (2013).
[34]N. Gaur *et al.*, "First-order reversal curve investigations on the effects of ion implantation in magnetic media," IEEE Trans. Magn. **48**, 2753 (2012).
[35]T. Hinoue *et al.*, "Effects of lateral straggling of ions on patterned media fabricated by nitrogen ion implantation," J. Appl. Phys. **111**, 07B912 (2012).
[36]B. D. Terris *et al.*, "Recording and reversal properties of nanofabricated magnetic islands," IEEE Trans. Magn. **41**(10), 2822 (2005).
[37]M. Nord *et al.*, "Strain anisotropy and magnetic domains in embedded nanomagnets," Small **15**, 1904738 (2019).
[38]A. Iwase *et al.*, "Study on irradiation-induced magnetic transition in FeRh alloys by means of Fe K-edge XMCD spectroscopy," Nucl. Instrum. Methods Phys. Res. **256**, 429–433 (2007).
[39]A. Heidarian *et al.*, "Tuning the antiferromagnetic to ferromagnetic phase transition in FeRh thin films by means of low-energy/low fluence ion irradiation," Nucl. Instrum. Methods Phys. Res. **358**, 251–254 (2015).
[40]S. Cervera *et al.*, "Modulating the phase transition temperature of giant magnetocaloric thin films by ion irradiation," Phys. Rev. Mater. **1**, 065402 (2017).
[41]D. G. Merkel *et al.*, "Reversible control of magnetism in FeRh thin films," Sci. Rep. **10**, 13923 (2020).
[42]S. P. Bennett *et al.*, "Magnetic order multilayering in FeRh thin films by He-ion irradiation," Mater. Res. Lett. **6**, 106–112 (2018).
[43]J. F. Ziegler, M. D. Ziegler, and J. P. Biersack, Nucl. Instrum. Methods Phys. Res., Sect. B **268**, 1818–1823 (2010).
[44]C. Q. Yu *et al.*, "Thickness-dependent magnetic order and phase-transition dynamics in epitaxial Fe-rich FeRh thin films," Phys. Lett. A **383**, 2424–2428 (2019).
[45]M. Björck and G. Andersson, "GenX: An extensible X-ray reflectivity refinement program utilizing differential evolution," J. Appl. Crystallogr. **40**, 1174 (2007).
[46]C. Baldasseroni *et al.*, "Effect of capping material on interfacial ferromagnetism in FeRh thin films," J. Appl. Phys. **115**, 043919 (2014).
[47]L. Zsoldos, "Lattice parameter change of FeRh alloys due to antiferromagnetic-ferromagnetic transformation," Phys. Status Solidi **20**, K25 (1967).
[48]C. Bordel *et al.*, "Fe spin reorientation across the metamagnetic transition in strained FeRh thin films," Phys. Rev. Lett. **109**, 117201 (2012).
[49]G. Filoti, V. Kuncsea, E. Navarro, A. Hernando, and M. Rosenberg, "Hyperfine fields and Fe magnetic moments in Fe-Rh alloys; a Mössbauer spectroscopy study," J. Alloys Compd. **278**, 60–68 (1998).
[50]L. Sandratskii and L. Mavropoulos, "Magnetic excitations and femtomagnetism of FeRh: A first-principles study," Phys. Rev. B **83**, 174408 (2011).
[51]A. van Veen *et al.*, "VEPFIT applied to depth profiling problems," Appl. Surf. Sci. **85**, 216 (1995).
[52]T. Kosub *et al.*, "Purely antiferromagnetic magnetoelectric random access memory," Nat. Commun. **8**, 13985 (2017).
[53]M. J. Puska and R. M. Nieminen, "Theory of positrons in solids and on solid surfaces," Rev. Mod. Phys. **66**, 841–897 (1994).
[54]M. Alatalo *et al.*, "Theoretical and experimental study of positron annihilation with core electrons in solids," Phys. Rev. B **54**, 2397–2409 (1996).
[55]R. Oshima *et al.*, "Positron annihilation study on defects and phase transition of FeRh alloys subjected to high-speed deformation," Radiat. Eff. Defects Solids **157**, 127–135 (2010).
[56]J. Čížek *et al.*, "Vacancy clusters in ultra fine grained metals prepared by severe plastic deformation," J. Phys. Conf. Ser. **443**, 012008 (2013).
[57]R. Krause-Rehberg and H. S. Leipner, *Positron Annihilation in Semiconductors: Defect Studies* (Springer, 1999).
[58]C. Bull *et al.*, "PNR study of the phase transition in FeRh thin films," APL Mater. **7**, 101117 (2019).
[59]C. Gatel *et al.*, "Inhomogeneous spatial distribution of the magnetic transition in an iron-rhodium thin film," Nat. Commun. **8**, 15703 (2017).
[60]R. Fan *et al.*, "Ferromagnetism at the interfaces of antiferromagnetic FeRh epilayers," Phys. Rev. B **82**, 184418 (2010).
[61]C. J. Kinane *et al.*, "Observation of a temperature dependent asymmetry in the domain structure of a Pd-doped FeRh epilayer," New J. Phys. **16**, 113073 (2014).
[62]S. P. Bennett *et al.*, "Direct evidence of anomalous interfacial magnetization in metamagnetic Pd doped FeRh thin films," Sci. Rep. **5**, 9142 (2015).
[63]V. von Hörsten, "Pi program package," available at: http://udue.de/Pi, 2020.
[64]M. O. Liedke *et al.*, "Open volume defects and magnetic phase transition in $Fe_{60}Al_{40}$ transition metal aluminide," J. Appl. Phys. **117**, 163908 (2015).
[65]W. Anwand *et al.*, "Design and construction of a slow positron beam for solid and surface investigations," Defect Diffus. Forum **331**, 25 (2012).
[66]J. V. Olsen *et al.*, "PALSfit: A new program for the evaluation of positron lifetime spectra," Phys. Status Solidi C **4**, 4004–4006 (2007).
[67]S. Tuomisto and I. Makkonen, "Defect identification in semiconductors with positron annihilation: Experiment and theory," Rev. Mod. Phys. **85**, 1583–1631 (2013).
[68]E. H. Khan, M. H. Weber, and M. D. McCluskey, "Formation of isolated Zn vacancies in ZnO single crystals by absorption of ultraviolet radiation: A combined study using positron annihilation, photoluminescence, and mass spectroscopy," Phys. Rev. Lett. **111**, 017401 (2013).
[69]W. Griggs *et al.*, "PNR determination of the magnetic depth profile in uniformly ion irradiated FeRh thin films," STFC ISIS Facil. (2019).